ACS Catalysis

Research Article

pubs.acs.org/acscatalysis

Propane Dehydrogenation over $Pt/TiO_2-Al_2O_3$ Catalysts

Feng Jiang, Liang Zeng, Shuirong Li, Gang Liu, Shengping Wang, and Jinlong Gong*

Key Laboratory for Green Chemical Technology of Ministry of Education, School of Chemical Engineering and Technology; Collaborative Innovation Center of Chemical Science and Engineering, Tianjin University, Tianjin 300072, China

Supporting Information

ABSTRACT: This paper describes an investigation on understanding catalytic consequences of Pt nanoparticles supported on a $TiO_2-Al_2O_3$ binary oxide for propane dehydrogenation (PDH). The $TiO_2-Al_2O_3$ supports were synthesized by a sol–gel method, and the $Pt/TiO_2-Al_2O_3$ catalysts were prepared by an incipient wetness impregnation method. Both as-prepared and post-experiment catalysts were characterized employing N_2 adsorption–desorption, X-ray diffraction, Raman spectra, H_2-O_2 titration, temperature-programmed desorption, thermogravimetric analysis, temperature-programmed oxidation, transmission electron microscopy, and Fourier-transform infrared spectra of chemisorbed CO. We have shown that TiO_2 is highly dispersed on Al_2O_3, and the addition of appropriate amount of TiO_2 improves propylene selectivity and catalytic stability, which is ascribed to the electron transfer from partially reduced TiO_x ($x < 2$) to Pt atoms. The increased electron density of Pt could reduce the adsorption of propylene and facilitate the migration of coke precursors from the metal surface to the support. The addition of TiO_2, however, also increases the amount of strong acid centers on the supports and the excessive TiO_2 addition might lead to a significant amount of coke formation. The electron transfer effect and the acid sites effect of TiO_2 addition exert an opposite influence on catalytic performance. The trade-off between the electron transfer effect and the acid sites effect is studied by varying the amount of TiO_2 loading. An optimal loading content of TiO_2 is 10 wt %, which results in a higher propylene selectivity and a better stability.

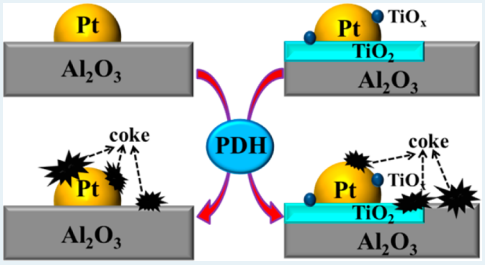

KEYWORDS: *propane dehydrogenation, $TiO_2-Al_2O_3$, electron transfer, C_3H_6 desorption, coke (precursors) migration*

1. INTRODUCTION

Propane dehydrogenation (PDH) is a commercial propylene production technology that has received much attention in recent years.[1,2] Propylene is an important building block for a large amount of petrochemicals including polypropylene, propylene oxide, and acrylonitrile.[3−5] PDH is a highly endothermic process, which requires an elevated reaction temperature to attain a desirable yield of propylene. However, the high reaction temperature results in major challenges of hydrocarbon cracking and coke formation, which reduce the selectivity to propylene and catalyst stability,[6] respectively.

Typically, the catalyst containing platinum nanoclusters as active components is widely used in commercial PDH processes.[7,8] Supported Pt catalysts show high catalytic activity and excellent thermal stability[9,10] with lower amount of coke deposits.[7] Despite these facts, catalyst deactivation due to coke formation remains challenging.[11−13] In addition, the severe reaction conditions lead to the generation of lighter hydrocarbons via C–C bond cleavage and the lower selectivity to propylene.[14,15] It is of great significance to develop Pt-based catalysts with high selectivity toward propylene and excellent anti-coking capability.

A number of strategies have been suggested to improve the catalytic performance of supported Pt catalysts, including the introduction of metal promoters.[13,16] For the dehydrogenation of light alkanes over supported Pt catalysts, the alkene selectivity increased and the tendency to coke formation decreased with the addition of metal promoters such as Sn, Zn, Ge, Pb, and Re.[9−12,17−20] There have been a number of studies on the effect of Sn in Pt–Sn catalysts. The modification of monometallic Pt by Sn enhances the dissociative adsorption of the reacting alkane and attenuates the adsorption of the product alkene,[21−24] which increases the formation rate of alkene and reduces the formation of lighter hydrocarbons and coke via dehydrogenation from readsorbed alkene.[25]

To further enhance the tolerance against catalyst deactivation, the incorporation of metal oxides has been confirmed as an effective method, including the oxides of alkali metal (Li, K, Ca),[26−28] and rare earth metal (La, Ce, Y).[29] The presence of these promoting metal oxides with different contents in Pt catalysts may result in changes in the coordination number, dispersion of metallic particles and/or neutralization of acid sites, which can influence the catalytic performance. However, the promoting effect of these metal oxides is limited because they afford less powerful metal–support interactions.[28] In earlier studies,[30,31] Tauster et al. described the strong metal–support interaction (SMSI) in Pt/TiO_2 catalysts ascribed to the electron transfer from partially reduced support to metal crystallites. In alkane dehydrogenation processes, the promoting effect of TiO_2 component could be more pronounced than

Received: August 28, 2014
Revised: December 4, 2014
Published: December 8, 2014

that of alkali and rare earth metal oxides owing to much stronger interaction between Pt and TiO_2. The major disadvantages associated with the TiO_2 support are its relatively low specific surface area and low thermal stability at high temperatures. However, these drawbacks could be overcome when TiO_2 is combined with thermally stable materials possessing high specific surface area (e.g., Al_2O_3). Several studies concerning TiO_2–Al_2O_3 binary oxides suggested that Al_2O_3 stabilized the structure of TiO_2 and afforded high specific surface area.[32,33]

This paper describes the utilization of TiO_2 to promote strong metal–support interaction between Pt and the support for improving the catalytic performance of Pt catalysts in PDH. A series of TiO_2–Al_2O_3 binary oxide supports were synthesized using the sol–gel method, and then the Pt/TiO_2–Al_2O_3 catalysts were prepared by the incipient wetness impregnation method. The interaction between TiO_2 and Pt particles and the influence of TiO_2 on the catalytic properties of supported catalysts in PDH were investigated. The as-prepared catalysts were characterized using various techniques, and the catalytic performance was investigated to understand the role of TiO_2 on catalytic properties of Al_2O_3 supported Pt catalysts. Furthermore, characterizations of spent catalysts were performed to investigate the nature of coke deposits on catalysts. Particular emphasis was focused on the electron transfer between Pt particles and TiO_2 species as well as the influence of electron transfer on the adsorption of products and the migration of coke precursors. The optimal loading of TiO_2 was also studied and discussed.

2. EXPERIMENTAL SECTION

2.1. Preparation of Supports and Pt Catalysts. The TiO_2–Al_2O_3 supports were prepared by the sol–gel method using HNO_3 as a hydrolysis catalyst. Aluminum tri-*sec*-butoxide (Alfa Aesar, 97.0%) and tetrabutyl titanate (Sinopharm Chemical Reagent Co., Ltd., 98.0%) used as organic precursors were dissolved in isopropanol with an appropriate amount of hexadecyl trimethylammonium bromide (CTAB) addition. After 2 h of continuous stirring, an aqueous solution of HNO_3 was dropwise added into the precursor solution, followed by a hydrolysis process for 0.5 h under vigorous stirring. Nominal molar ratios utilized were water/isopropanol/acid/CTAB/alkoxide = 20:6:0.2:0.05:1. The obtained alcogels were ripened for a 24 h period, followed by vacuum drying at 70 °C for 18 h. Finally, the gels were held at 250 °C for 2 h and calcined at 600 °C for 4 h. The solids prepared were named TAx, where x is the weight ratio of $TiO_2/(TiO_2 + Al_2O_3)$.

Supported Pt catalysts were prepared by the incipient wetness impregnation method to obtain 1 wt % Pt loading. The precursor used was $H_2PtCl_6{\cdot}6H_2O$ (Tianjin Kaiyingte chemical trade Co., Ltd., 99.9%) in an aqueous solution. The synthesized TAx supports were impregnated in the H_2PtCl_6 solution at room temperature for 12 h. After metal deposition, the impregnated solids were dried at 90 °C overnight, and then calcined at 600 °C for 3 h.

2.2. Characterization. XRD measurements were performed with 2θ values between 20 and 80° by using a Rigaku C/max-2500 diffractometer employing the graphite filtered Cu Kα radiation (λ = 1.5406 Å).

Raman spectra were obtained under ambient conditions using a Renishaw inVia Reex Raman spectrometer with a 532 nm Ar-ion laser beam. Data acquisition was conducted with an exposure time of 10 s and 1 accumulation.

Textual properties of the supports and catalysts were measured with a Micromeritics Tristar 3000 analyzer by nitrogen adsorption at −196 °C. The samples were outgassed at 300 °C for 4 h before measurements. This instrument employed the Brunauer–Emmett–Teller (BET) method by measuring the quantity of nitrogen absorbed at −196 °C and the cumulative pore volumes and pore sizes were obtained by the Barrett–Joyner–Halenda (BJH) method from the desorption branches of the adsorption isotherms.

NH_3-TPD experiments were carried out to analyze the acidic properties of the supports using a Micromeritics AutoChem 2920 apparatus. Prior to NH_3 adsorption, 100 mg sample was pretreated at 300 °C for 1 h under Ar stream (20 mL/min). After cooling to 100 °C, NH_3 was adsorbed using a flow of 10 vol % NH_3/N_2 (30 mL/min) for 0.5 h. The NH_3 desorption was performed in He (20 mL/min) with a heating rate of 10 °C/min and the NH_3 desorption profile was registered with a thermal conductivity detector.

Dispersion of platinum was studied employing the hydrogen–oxygen titration method.[34] For each test, 200 mg sample was reduced with 10 vol % H_2/Ar at 500 °C for 1 h, then cooled to 50 °C, following which oxygen was admitted to the sample by injection pulses of 10 vol % O_2/He (0.5082 mL) until the consumption peaks became stable. Subsequently, the H_2 chemisorption was carried out at the same temperature by injection pulses of 10 vol % H_2/Ar (0.5082 mL). It can be assumed that the adsorption stoichiometry factor of Pt/H_2 = 2/3.[34,35] The metal dispersion is calculated using the following equation:

$$\text{Dispersion}\ (\%) = \frac{V_{H_2} \times \text{SF} \times \text{MW}_{Pt}}{W_{Pt} \times 22414} \times 100 \quad (1)$$

where V_{H_2} is the volume of adsorbed H_2 (mL), SF is the stoichiometry factor, MW_{Pt} is the atomic weight of Pt (g mol^{-1}), and W_{Pt} is the weight of supported Pt on the sample (g).

TEM was conducted to characterize the morphology of catalysts using a JEM-2100F transmission electron microscope at 200 kV. The fresh catalysts were prereduced at 500 °C in a flow rate of 50 mL min^{-1} of 20 vol % H_2/N_2 for 1 h before characterization. The samples were dispersed in ethanol and supported on carbon-film-coated copper grids before TEM images were recorded.

TGA (STA449F3 NETZSCH Corp.) was used to investigate the carbon deposition of spent catalysts. The sample was preheated at 80 °C for 0.5 h in N_2 (50 mL/min). Then the sample was heated to 800 °C at a rate of 10 °C/min in air (100 mL/min).

TPO was carried out by using a Micromeritics AutoChem 2920 apparatus equipped with a HIDEN QIC-20 mass spectrometer (MS). The spent catalyst (100 mg) was pretreated at 200 °C for 1 h under flowing Ar (30 mL/min). Upon cooling to 100 °C, a flow rate of 30 mL/min of air was used for oxidation, and the temperature was increased linearly from 100 to 800 °C at 10 °C/min. The CO_2 in the effluent was monitored and recorded online by MS.

Fourier-transform infrared (FT-IR) spectra of chemisorbed CO on activated catalysts were collected on a Nicolet 6700 spectrometer using a stainless steel cell connected to a gas-dosing and evacuation system. In a typical procedure, 30 mg of as-calcined catalyst was compressed into a 13 mm diameter self-supporting wafer and carefully loaded into in situ cell equipped

dx.doi.org/10.1021/cs501279v | ACS Catal. 2015, 5, 438–447

Table 1. Physical Properties of Catalysts

samples	BET surface area (m^2/g)	average pore diameter (nm)	pore volume (cm^3/g)	particle size[a] (nm)	particle size[b] (nm)	metal dispersion[b] (%)	metal surface area[b] ($m^2/g_{cat.}$)
TA0	315	0.68	6.4	--	--	--	
TA10	321	0.70	6.3	--	--	--	
TA20	337	0.76	6.5	--	--	--	
Pt/TA0	273	0.65	6.8	2.2 ± 0.3	2.7	41.9	1.0
Pt/TA10	293	0.71	6.6	2.1 ± 0.2	2.5	45.8	1.1
Pt/TA20	285	0.75	7.1	2.3 ± 0.3	2.6	44.1	1.1
Pt/TA0(spent)	282	0.57	6.0	2.1 ± 0.1	--	--	
Pt/TA10(spent)	255	0.53	5.7	2.3 ± 0.2	--	--	
Pt/TA20(spent)	228	0.43	5.4	2.3 ± 0.2	--	--	

[a]Determined by TEM images. [b]Determined by H_2-O_2 titration method.

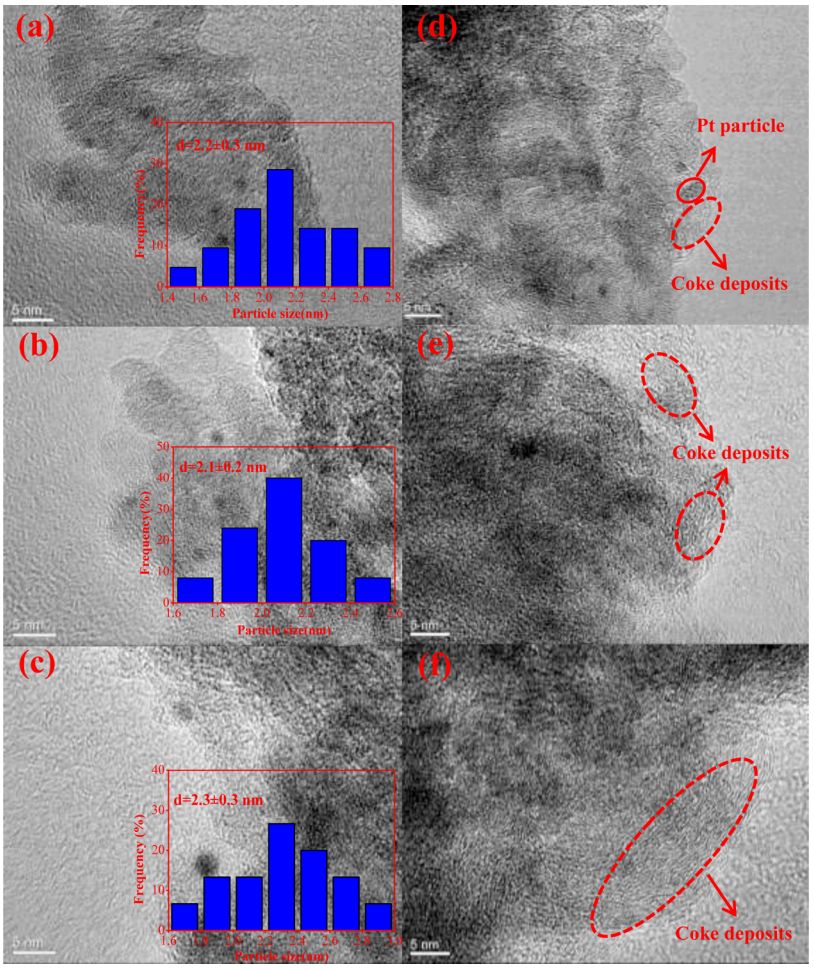

Figure 1. TEM images of reduced and spent catalysts, the insets are catalysts particle size distribution. (a) Pt/TA0, (b) Pt/TA10, (c) Pt/TA20, (d) Pt/TA0-spent, (e) Pt/TA10-spent, and (f) Pt/TA20-spent.

with ZnSe windows. The catalyst wafer was reduced under a flow of H_2 (30 mL/min) at 500 °C for 1 h followed by purging He (20 mL/min) for 0.5 h to completely remove the chemisorbed hydrogen species, and then cooled to 30 °C for collecting the background spectrum. Afterward, the sample was exposed to a flow of CO (10 mL/min) at 30 °C for 0.5 h. IR spectra were collected after purging He (30 mL/min) for 0.5 h and referenced to the background spectrum of reduced catalyst. Four scans were averaged using a resolution of 4 cm^{-1}.

C_3H_6-TPD experiments were performed on a Micromeritics AutoChem 2920 apparatus to determine the desorption energy of C_3H_6.[36] Prior to C_3H_6 adsorption, 150 mg of sample was reduced with 10 vol % H_2/Ar at 500 °C for 1 h, and C_3H_6 (99.5%) was adsorbed for 0.5 h after cooling to 50 °C. After purging He (30 mL/min) for 1 h, the temperature was ramped up to 500 °C with various heating rates, including 2, 5, 7, 10, 15, and 20 °C/min. The C_3H_6 desorption profiles were registered with a thermal conductivity detector. A plot of $\ln(\beta/T_p^2)$ versus $1/T_p$ for measurements made at different heating rates should be linear employing the following equation:[37]

$$\ln\left(\frac{\beta}{T_{p^2}}\right) = -\frac{E_d}{R \times T_p} + \ln\left(\frac{E_d \times A}{R \times C}\right) \quad (2)$$

dx.doi.org/10.1021/cs501279v | ACS Catal. 2015, 5, 438−447

where β represents the heating rate (K/min), T_p represents the desorption peak temperature (K), E_d represents the desorption energy of C_3H_6 (kJ/mol), A represents the quantity adsorbed at saturation state (cm^3/g, STP), R represents the gas constant (kJ/(mol·K)), and C is the related constant. Consequently, the desorption energy of C_3H_6 can be calculated from the slope of the fitting line.

2.3. Catalytic Tests. Catalytic tests were carried out at the atmospheric pressure and 600 °C in a quartz fixed-bed reactor with 8 mm inner diameter and 24 cm length. A mixture of 150 mg catalysts and 0.1 mL quartz sand with 20−40 mesh size distribution was loaded in the quartz tubular reactor. Prior to the test, the catalysts were reduced at 500 °C in situ for 1 h in a flow of 10 vol % H_2/N_2. Afterward, H_2/N_2 was replaced by the PDH reaction mixture of C_3H_8 (26 vol %) and H_2 (26 vol %) in N_2 at a total flow of 50 mL/min. The weight hourly space velocity (WHSV) of propane was 10 h^{-1}. The product gas was analyzed by an online GC equipped with a flame ionization detector (Chromosorb 102 column) and a thermal conductivity detector (Al_2O_3 Plot column).

The conversion of propane was determined from eq 3, and the selectivity to product was determined from eq 4:

$$\text{Conv}\ (\%) = \frac{[F_{C_3H_8}]_{in} - [F_{C_3H_8}]_{out}}{[F_{C_3H_8}]_{in}} \times 100 \quad (3)$$

$$\text{Sel}\ (\%) = \frac{n_i \times [F_i]_{out}}{\sum n_i \times [F_i]_{out}} \times 100 \quad (4)$$

where i represents the hydrocarbon product in the effluent gas, n_i is the number of carbon atoms of component i, and F_i is the corresponding flow rate.

A first-order deactivation model was used to investigate the catalytic stability,:[38]

$$k_d = \frac{\ln\left(\frac{100 - \text{Conv}_{600}}{\text{Conv}_{600}}\right) - \ln\left(\frac{100 - \text{Conv}_{20}}{\text{Conv}_{20}}\right)}{t} \quad (5)$$

where Conv_{20} and Conv_{600} represent the conversions at the start and the end of an experiment, respectively, t is the duration of experiment (h), k_d is the deactivation constant (h^{-1}). Higher k_d values are indicative of rapid deactivation.

3. RESULTS

3.1. Characterization of As-Prepared Catalysts. Physical properties of $TiO_2-Al_2O_3$ supports and Pt/TAx catalysts are presented in Table 1. The TiO_2 loading of Pt/TAx catalysts to be investigated is in the range of 0−20 wt % according to the catalytic performance analysis discussed later. The BET surface areas of TAx supports are higher than 300 m^2/g due to the specific preparation method and the introduction of CTAB (the surface area of TiO_2 is 29 m^2/g). Additionally, the pure TAx supports exhibit an appropriate pore size and pore volume distribution, which facilitates the dispersion of active metal nanoparticles. The impregnation of Pt causes a slight decrease in the specific surface area. The average Pt crystallite diameter determined by TEM images (the TEM images of fresh catalysts are shown in Figure 1) and the H_2-O_2 titration method are also shown in Table 1, together with the metal dispersion calculated based on eq 1. It can be observed that the Pt/TAx catalysts present similar Pt particle size and metal dispersion (about 41−45%), though small discrepancy exists between TEM images and the H_2-O_2 titration method. It is apparent that the doping of TiO_2 has a negligible influence on the particle size and the dispersion of platinum.

In order to investigate the structure of Pt/TAx catalysts and the distribution of TiO_2 on $TiO_2-Al_2O_3$ supports, the Pt/TA30, Pt/TA50, and Pt/TA100 catalysts were prepared as well. Diffraction patterns of as-prepared Pt/TAx catalysts are presented in Figure 2. The diffraction peaks at 2θ = 45.8°

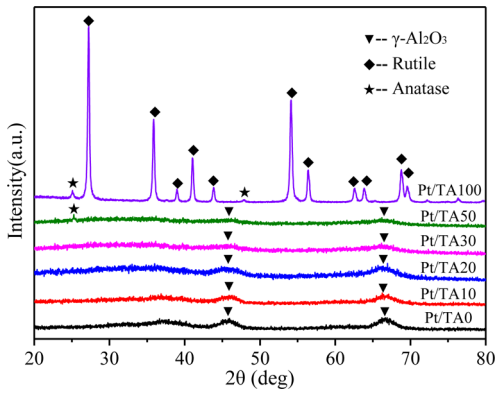

Figure 2. XRD patterns of Pt/TAx catalysts.

and 66.8° are assigned to γ-Al_2O_3. For TiO_2, diffraction peaks at 2θ = 25.3° and 48.0° are assigned to anatase, and the peaks at 2θ = 27.2°, 35.9°, 41.0°, 54.1°, 56.4°, and 68.7° are attributed to rutile TiO_2. For the Pt/TA100 catalyst, the diffraction peaks of rutile are detected as the main phase of TiO_2, suggesting that calcination at 600 °C leads to the coexistence of anatase and rutile. For the Pt/TA50 catalyst, however, the characteristic peaks of rutile are not detectable, and only the peaks of anatase and γ-Al_2O_3 are detected. Additionally, the peak intensities of γ-Al_2O_3 weaken with the increasing loading of TiO_2, and no diffraction peak of TiO_2 is detected until its content reaches 50 wt %.

For the $TiO_2-Al_2O_3$ binary oxide supports prepared by the sol−gel method or coprecipitation method, according to previous studies, the enrichment of TiO_2 on support surface is obtained.[32,33] Taking into account the fact that the surface free energies of TiO_2 (0.28−0.38 J/m^2) are significantly less than those of Al_2O_3 (0.65−0.93 J/m^2),[39,40] the dispersion of TiO_2 on the surface of Al_2O_3 is favored.[32] The XRD results suggest that TiO_2 is well dispersed on Al_2O_3 and no characteristic peak of TiO_2 can be detected when its loading is below 30 wt %. Therefore, TiO_2 is present in a highly dispersed state on the surface of Al_2O_3 when TiO_2 content is between 0 and 30 wt %. For the Pt/TA50 catalyst, the characteristic peaks of rutile are not detectable but the peaks of anatase are detected (both are detected for the Pt/TA100 catalysts). This indicates clearly that Al_2O_3 improves the thermal stability of TiO_2 and thus protects anatase TiO_2 from changing to rutile phase, which is in consistence with the literature.[41,42] For all the Pt/TAx catalysts, no diffraction peaks of Pt are detected, revealing that Pt is highly dispersed on the as-prepared $TiO_2-Al_2O_3$ supports and the particle size of Pt is extremely small, which is in accordance with the results presented in Table 1.

To further verify the crystalline phase of Pt/TAx catalysts with different TiO_2 contents and the TiO_2 distribution on the support surface, Raman spectra were acquired as shown in Figure 3. The band at 151 cm^{-1} is assigned to anatase TiO_2, and the bands at 245, 453, and 617 cm^{-1} are the characteristic

dx.doi.org/10.1021/cs501279v | ACS Catal. 2015, 5, 438−447

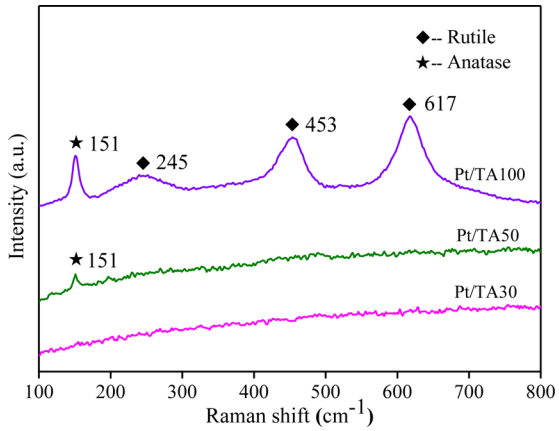

Figure 3. Raman spectra of Pt/TAx catalysts.

bands of rutile TiO_2.[43,44] For the Pt/TA100 catalyst, both the anatase and rutile phases are present in TiO_2, which correlates with the diffraction peaks of anatase and rutile in the XRD pattern of the Pt/TA100 sample. Nevertheless, the rutile phase of TiO_2 is not detected for the TA50 sample, indicating that the presence of Al_2O_3 retards the anatase-to-rutile phase transformation. When the TiO_2 loading is less than 30 wt % (the Raman spectra of Pt/TA20 and Pt/TA10 samples are not shown), no TiO_2 Raman band is observed, which is consistent with the literature.[45,46] Hence, for the TA10 and TA20 supports, highly dispersed TiO_2 on the surface of Al_2O_3 is obtained, and TiO_2 exhibits no crystalline phase.

NH_3-TPD profiles of Pt/TAx catalysts are depicted in Figure 4. To compare with each other, all the results were normalized.

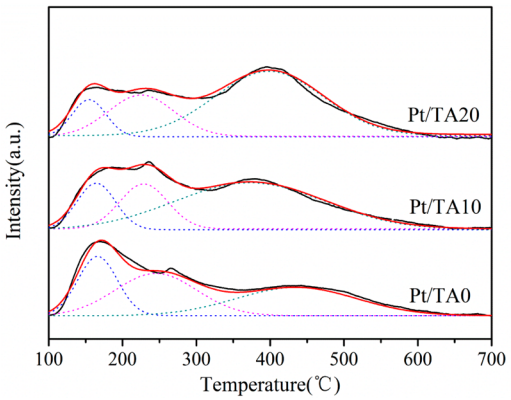

Figure 4. NH_3-TPD profiles of Pt/TAx catalysts.

The NH_3-TPD profiles of Pt/TA0 catalyst display three desorption peaks with maximal temperatures (T_M) at 166 °C, 247 and 432 °C. The T_M of the desorption peaks for Pt/TA10 and Pt/TA20 catalysts are 164 °C, 227 °C, 381 and 153 °C, 223 °C, 396 °C. As is known, the NH_3 desorptions in the temperature regions of 120−200 °C, 200−350 °C, 350−450 °C were regarded as the weak, medium, and strong acid sites, respectively.[47] To obtain the semiquantitative results of total acidity and the distribution of acidic strength, a Gaussian peak fitting method was adopted to deconvolute the NH_3-TPD curves.[48] The fitted peaks and fitting results are presented in Figure 4 and in Table 2, respectively. The peak areas correspond to the amount of acid centers. The total peak areas for Pt/TA0, Pt/TA10, and Pt/TA20 catalysts are 64.1, 71.2, and 80.1, respectively. The areas of three different peaks for Pt/TA0 catalyst are 16.2, 24.1, and 23.8. For Pt/TA10 catalyst, the areas are 12.3, 14.9, and 44.0; whereas these are 10.4, 19.4, and 50.3 for Pt/TA20 catalyst. Notably, it is revealed that the amount of strong acid centers increases significantly and the amount of weak acid centers decreases with the increasing TiO_2 content; the amount of medium acid centers increase with the increasing TiO_2 content when TiO_2 loading is higher than 10 wt %. Overall, the addition of TiO_2 results in the increase in the total amount of acid centers. The increment in strong acidity is due to the formation of bridged hetero metal−oxygen bonds (e.g., Ti−O−Al bonds) resulting in excessive charges.[49]

3.2. Catalytic Performance. The catalytic performance of Pt/TAx catalysts is depicted in Figure 5, which shows the variation of propane conversion and propylene selectivity as a function of time on stream. The pure support effect was also studied in blank tests, where propane conversions for all the TAx supports are about 5%. The initial propane conversions for Pt/TA0, Pt/TA10, and Pt/TA20 catalysts are 50.5%, 47.3%, and 45.5%; after 10 h of time on stream, these values decrease to 21.0%, 25.9%, and 17.8%, respectively. Consequently, the values of deactivation constant k_d (h^{-1}) for Pt/TA0, Pt/TA10 and Pt/TA20 catalysts are 0.13, 0.09, and 0.14. When the TiO_2 loading is up to 30 wt %, the Pt/TA30 catalyst encounters much more severe deactivation as conversion decreases to 17.9% upon 5 h of time on stream. Hence, the TiO_2 loading of Pt/TAx catalysts to be investigated is in the range of 0−20 wt %. Despite a slight decrease in the initial propane conversion, the addition of appropriate amount of TiO_2 (e.g., 10 wt %) in Pt/Al_2O_3 catalysts distinctly suppresses the deactivation and thus improves the stability. An increased selectivity of the catalyst is also observed at the beginning of the reaction as well as at the steady state after 3 h on stream. After 10 h on stream, the propylene selectivity for the Pt/TA0, Pt/TA10, and Pt/TA20 catalysts are 78.5%, 89.5%, and 92.7%, respectively. Notably, the selectivities toward light hydrocarbons (mainly methane and ethane) decrease severely with the increase of TiO_2 content, which means that the TiO_2 addition suppresses cracking reactions effectively. The 10 wt % TiO_2 addition contributes to a significant enhancement in propylene selectivity and catalyst stability. Excessive TiO_2 addition (20 wt %) has a negative influence on the catalytic stability. The optimal loading content of TiO_2 is determined to be 10 wt %, which results in a high propylene selectivity of 89.5% and a better stability.

Table 2. Fitted Results of NH_3-TPD Experiments of Pt/TAx Catalysts

	T_M (°C)				peak area (a.u.)			
samples	I	II	III	total area (a.u.)	I	II	III	fitted parameter, R^2
Pt/TA0	166	247	432	64.1	16.2	24.1	23.8	0.99
Pt/TA10	164	227	381	71.2	12.3	14.9	44.0	0.99
Pt/TA20	153	223	396	80.1	10.4	19.4	50.3	0.99

dx.doi.org/10.1021/cs501279v | ACS Catal. 2015, 5, 438−447

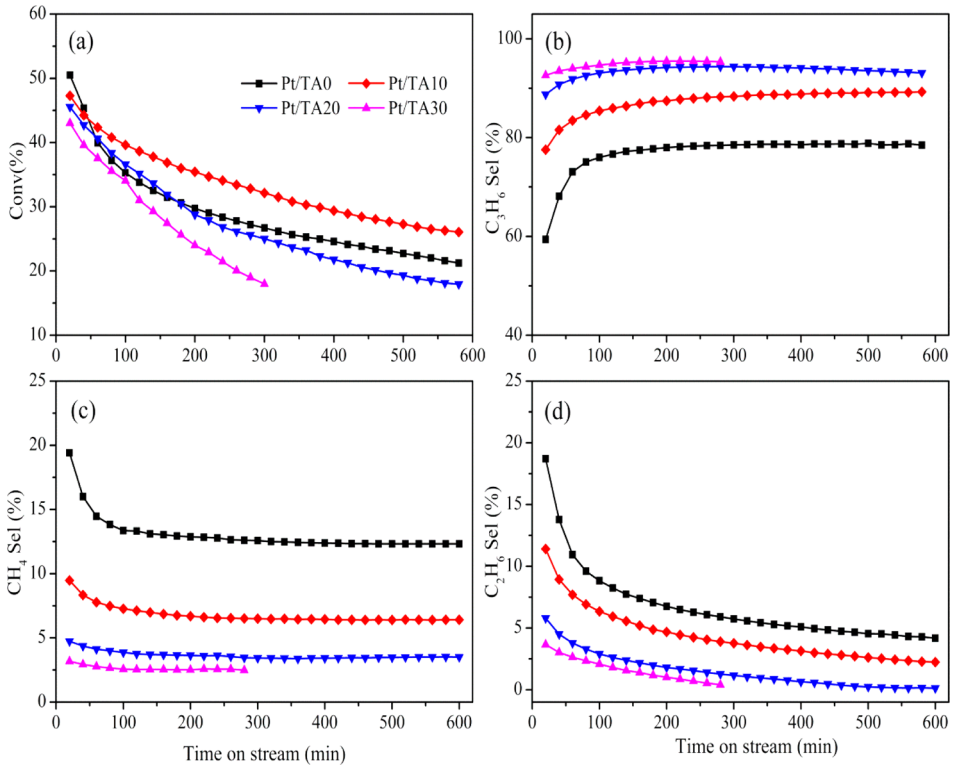

Figure 5. Catalytic activity and selectivity of Pt/TAx catalysts in propane dehydrogenation. (a) Conversion of C_3H_8; (b) selectivity to C_3H_6; (c) selectivity to CH_4; (d) selectivity to C_2H_6 (T = 600 °C, atmospheric pressure, WHSV propane = 10 h^{-1}, 150 mg of catalyst, C_3H_8/H_2 = 1/1, with balance N_2 for total flow rate of 50 mL/min).

3.3. Structure of Spent Catalysts. TEM images of spent catalysts are illustrated in Figure 1. The Pt particle sizes of spent catalysts are presented in Table 1. Apparently, negligible change in Pt particle size occurred upon the catalytic reaction. The substances with nonuniform structure shown in the images (inside the red dotted circles), which shows distinctly different morphologies from the supports, can be assigned to coke deposits. The disordered structure of the coke deposits is ascribed to the amorphous coke. It is well established that coke formation is the main culprit for catalyst deactivation. For the spent catalysts, it can be clearly observed that the amount of coke deposits increases with the addition of TiO_2. For Pt/TA10 and Pt/TA20 catalysts, as exhibited in Figure 1e,f, the coke deposits are mainly located on the support instead of covering the Pt particles. That will afford more active sites than Pt/TA0 catalyst.

The amount of deposited carbon was quantitatively determined by TGA in an oxidizing environment, and the mass loss profiles are shown in Figure 6. From these profiles, it can be observed that the amount of coke deposition follows the order Pt/TA0 (10.6%) < Pt/TA10 (14.7%) < Pt/TA20 (18.4%). The addition of TiO_2 contributes to higher amount of coke deposits. This outcome is due to the enhancement of acidity for the Pt/TA10 and Pt/TA20 catalysts. The enhancement of acidic strength, particularly the increase of strong acid sites, promotes side reactions such as isomerization, cyclization and coking.[48] To further investigate the amount and location of coke deposits, TPO measurements were performed and the concentration of CO_2 was detected by MS and shown in Figure 7. Two peaks are observed in TPO profiles, where the first peak is due to the coke on the metal sites, and the second one is from the coke on the support.[12,50] Coke and coke precursors

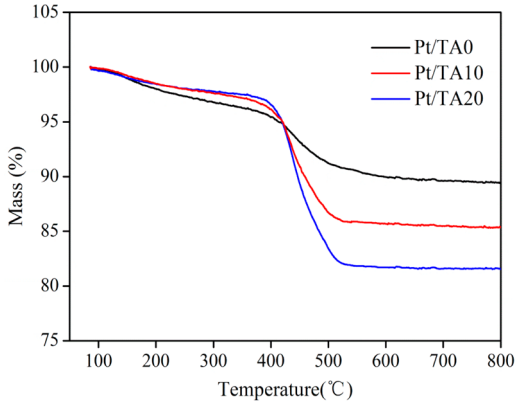

Figure 6. TGA profiles for the spent catalysts.

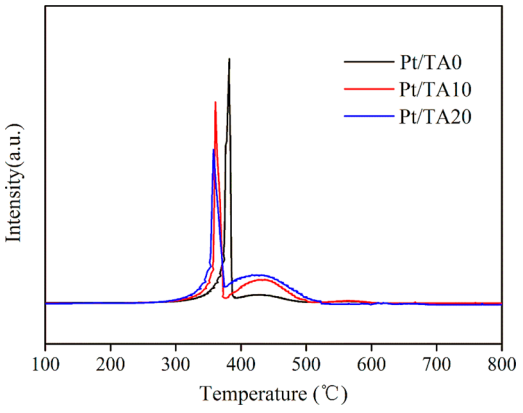

Figure 7. TPO results for the spent catalysts.

dx.doi.org/10.1021/cs501279v | ACS Catal. 2015, 5, 438−447

are initially formed on the metal surface and then transferred to the support, followed by further dehydrogenation and condensation reactions on acid sites.[51,52] Therefore, more heavily condensed coke species are expected to be formed on the support, which might be more difficult to be removed through combustion as higher oxidation temperature is required.

The TPO curves are normalized and the peak areas correspond to the amount of deposited carbon. The semi-quantitative analyses of the coke deposits distribution were achieved by quantifying the peak areas, and the results are incorporated in Table 3. The total peak area for the Pt/TA0 catalyst is 39.7, whereas those are 50.5 and 63.9 for the Pt/TA10 catalyst and Pt/TA20 catalyst, respectively. Additionally, the areas of the first and second peaks are 32.3 and 7.4 for the Pt/TA0 catalyst. For the Pt/TA10 catalyst, the areas are 28.0 and 22.5, respectively; for the Pt/TA20 catalyst, the areas are 24.8 and 39.1. It can be concluded that less coke is formed on the metal surface for the Pt/TA10 catalyst and Pt/TA20 catalyst than it does for the Pt/TA0 catalyst, even though much more coke is located on the support for the former. This demonstrates that the addition of TiO_2 facilitates the migration of coke and coke precursors from metal to the support.

Table 3. Results of TPO Experiments for Spent Catalysts

	T_M (°C)			area	
spent catalysts	I	II	total area (a.u.)	I	II
Pt/TA0	383	426	39.7	32.3	7.4
Pt/TA10	361	431	50.5	28.0	22.5
Pt/TA20	358	427	63.9	24.8	39.1

4. DISCUSSION

The observed influence of the appropriate amount of TiO_2 addition on propylene selectivity and catalytic stability can be explained by electronic and geometric effects of partially reduced TiO_x species. The slightly decreasing initial conversion with the increasing TiO_2 addition is caused by the partial encapsulation effect of TiO_x species.[31,53] Similar to Pt−Sn catalysts,[54,55] electron transfer from TiO_x species to Pt most likely hinders propylene adsorption on metal sites and consequently decreases the likelihood of deep dehydrogenation and hydrogenolysis. To verify the changes in the electronic environment of nearby Pt atoms caused by TiO_2 addition and its influence on C_3H_6 desorption and coke precursor migration, the FT-IR experiments of adsorbed CO and C_3H_6-TPD experiments were performed and then discussed.

4.1. Electronic Environment Near Pt Study by FT-IR of Adsorbed CO. The electronic environment nearby Pt atoms was investigated using IR spectroscopy with CO as the probe molecule (Figure 8). The adsorbed CO on the Pt/TA0 catalyst clearly shows a sharp peak, which corresponds to CO that is linearly bonded onto surface Pt atoms. The linear adsorption peak of the catalyst can be resolved into two peaks. The higher energy band at around 2072 cm^{-1} is associated with the CO linearly bound to the terraces or planes that are coordinatively saturated, while the broad band around 2043 cm^{-1} is assigned to the CO adsorbed at the corners or steps that are coordinatively unsaturated.[56,57] In comparison with the Pt/TA0 catalyst, the presence of 10 wt % TiO_2 results in a downward shift of CO band to 2062 and 2033 cm^{-1}; furthermore, the addition of 20 wt % TiO_2 results in a downward shift to 2056 and 2022 cm^{-1}. Several reasons could account for the frequency shift of the linear CO adsorption peak with increasing amount of TiO_2 content, including the variation in the average size of Pt particles and the interaction between Pt and TiO_2 species acting as electron donor.[28] However, the average sizes of Pt particles for Pt/TA0, Pt/TA10, and Pt/TA20 catalysts are fairly similar (Table 1), which excluded the size effect in this case.

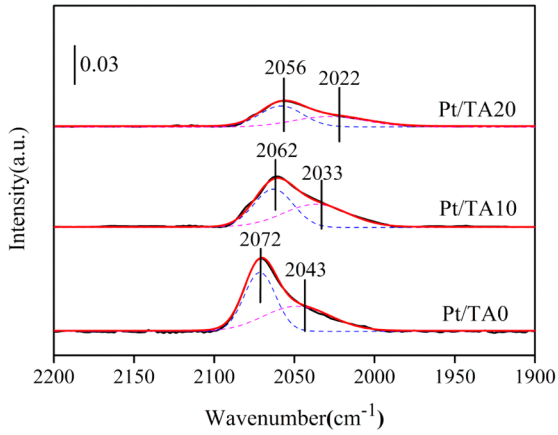

Figure 8. IR spectra of chemisorbed CO on reduced Pt/TAx catalysts.

The bonding between CO and the metal is formed by the electron donation from the CO 5σ orbital to the empty d orbital of the metal, and the back-donation from the filled metal d orbital to the CO 2π* antibonding orbital of the CO molecules. According to previous reports, strong metal support interaction (SMSI) appeared when Pt/TiO_2 catalyst was reduced at high temperatures such as 500 °C, where the presence of Pt catalyzed the partial reduction of TiO_2 to form TiO_x ($x < 2$).[58] The SMSI behavior was explained by two aspects: the electron transfer from partially reduced TiOx species to Pt and the partial coverage of the metal surface by TiO_x species.[31,53] The frequency shift presented in Figure 8 strongly indicates an increased electron density over the Pt atoms owing to the electron transfer from the TiO_x species. The higher Pt electron density increases the back-donation into the 2π* antibonding orbital of CO molecules as electron-acceptor species, which leads to a strengthening of the Pt-CO bond and a weakening of the C−O bond (red shift of CO stretching frequency).[18,59] The ratio of the integrated peak area for CO to the integrated peak area for an Al−O vibrational mode could be a good basis of comparison for the amount of CO adsorbed. Because the intensities of Al−O vibration peaks remain close to each other (shown in Figure S2), the peak intensities of the CO were applied to stand for the amount of adsorbed CO instead of the ratio between the integrated peak area for CO and the integrated peak area for a Al−O vibration. It is observed that the peak intensity decreases notably with the increasing TiO_2 content (the peak intensities of Pt/TA0, Pt/TA10, and Pt/TA20 catalysts are 0.086, 0.065, and 0.033, respectively) which is caused by the partial coverage of Pt surface by TiO_x species migrating from the support onto metal particles.

The interplay between the metallic sites and coke deposits determines the mobility of coke.[60] Propylene, acting as electron-donor, transfers electron to the empty d orbital of Pt.[28,61] Thus, the high electron density of Pt particles is beneficial to weaken Pt-(C═C) bonds,[60] as well as to repulse

dx.doi.org/10.1021/cs501279v | ACS Catal. 2015, 5, 438−447

the coke precursors and the desired product propylene. The increased electron density of Pt particles promotes the desorption of C_3H_6 and thus suppresses the further dehydrogenation and C−C cleavage causing low propylene selectivity; the high electron density of Pt atoms weakens the interaction between Pt and coke precursors, boosts the migration of coke precursors from Pt sites to support, and lastly, enhances the catalytic stability against coke deposit significantly.

4.2. Coke Precursor and Product Interaction with Pt/TAx by C_3H_6-TPD. The interactions of propylene with the Pt/TAx catalysts were examined by the means of C_3H_6-TPD. The desorption spectra are presented in Figure 9 (the spectra of

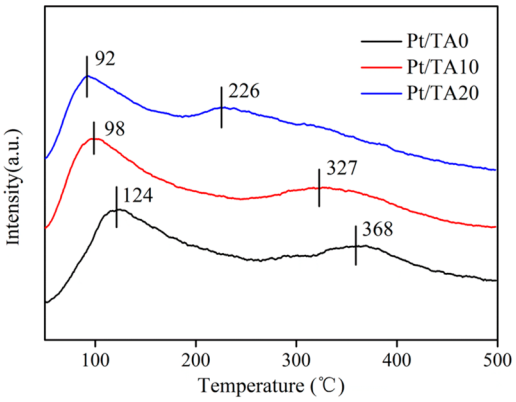

Figure 9. C_3H_6-TPD profiles of fresh Pt/TAx catalysts (heating rate β = 5 °C/min).

heating rate β = 5 °C/min are taken to show examples, the others are not shown here). The desorption profiles exhibit two peaks which are assigned to the C_3H_6 adsorbed with different strength. The TPD measurements clearly show that the propylene adsorbed on the catalysts is released at different temperatures. The desorption temperature can be used to evaluate the interactions between propylene and samples. Obviously, the desorption peaks of propylene over Pt/TAx catalysts shift to lower temperatures as the TiO_2 addition increases. The TiO_2 component tends to decrease the interactions between propylene and catalysts, indicating that the addition of TiO_2 weakens the adsorption of propylene and thereby decreases the amount of adsorbed propylene.[62] The C_3H_6-TPD experiments over the used catalysts were also performed (shown in Figure S3). For spent catalysts with coke deposits, it is obvious that the desorption peak shifted to lower temperatures indicating weaker interactions between propylene and catalysts. It seems that the coke formation tends to increase the selectivity toward propylene along with time on stream owing to better ability to repulse propylene, which is consistent with the experimental results in Figure 5.

In order to compare the desorption kinetics of adsorbed propylene, the values of the desorption energy E_d have been determined. Analysis of TPD measurements made with varying heating rates, β, allows the calculation of E_d through eq 2. The plots of $\ln(\beta/T_p^2)$ versus $1/T_p$ are shown in Figure 10. Values of desorption energy for the Pt/TA0, Pt/TA10, and Pt/TA20 catalysts are 64 ± 8, 45 ± 9, and 33 ± 4 kJ/mol, respectively. The value of desorption energy decreases significantly with the increasing TiO_2 content, suggesting that the addition of TiO_2 promotes the desorption of propylene, which is clearly shown in Figure 9. The promoted desorption of propylene is

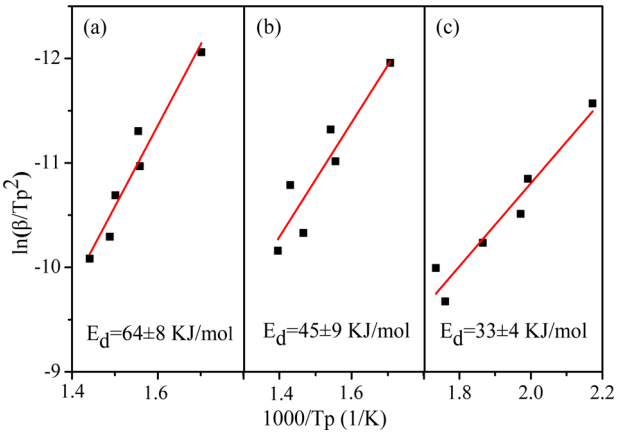

Figure 10. C_3H_6 desorption energy over fresh Pt/TAx catalysts calculated from the slope of fitting line. (a) Pt/TA0; (b) Pt/TA10; (c) Pt/TA20.

attributed to the electron donation from TiO_x species to Pt particles as proved by FT-IR spectra of adsorbed CO (Figure 8). With the addition of TiO_2, the electron-rich Pt particles tend to repulse the electron-rich propylene as well as the coke precursors. It is concluded that the promoted desorption of propylene prevents propylene from converting to deep dehydrogenation products and thereby increases the propylene selectivity in PDH. Furthermore, the enhanced desorption of electron-rich coke precursors (including propylene) promotes the coke precursors migration from Pt sites to support and affords more efficient exposure of active sites—lastly improving the catalytic stability against coke formation.

Hence, propylene selectivity is raised to a large extent with increasing TiO_2 content due to the electronic environment changes near Pt particles. The increased electron density of Pt atoms also accelerates the removal of coke precursors from Pt particles and facilitates the transfer of coke deposits from active sites to the support. The TPO results have confirmed that the addition of TiO_2 facilitates the migration of coke and coke precursors from metal to the support. Though TiO_2 addition contributes to higher amount of coke deposits due to enhanced acidity on the support, only the part of coke belonging to the metal surface is mainly responsible for the deactivation of active sites,[12] the coke on the support is less related to the deactivation of the main reaction. Less coke on Pt affords more exposed active sites, which can explain the enhanced stability for the Pt/TA10 catalyst. This is consistent with the study on Pt−Sn/Al_2O_3 catalysts,[12,63] where the coke formation on Pt sites in the bimetallic sample is apparently less than that in the corresponding monometallic one, although the total amount of coke deposits over the bimetallic catalyst (including support) is even higher. Therefore, higher catalytic stability is obtained for the Pt/TA10 catalyst than it is for the Pt/TA0 catalyst, though a higher amount of coke deposits are produced.

However, excessive introduction of TiO_2 (e.g., 20 wt %) results in severe deactivation. Different from the coverage of Pt sites by coke, this may be due to the serious blockage of catalyst pores other than Pt sites by vast amount of coke deposits cutting off reactant molecules access to the pores.[3,64] It can be observed from Table 1 that the specific surface areas of spent catalysts are 282, 255, and 228 m^2/g, respectively. The specific surface areas of spent Pt/TAx catalysts decrease sharply with the increasing TiO_2 content, suggesting much more serious coverage and blockage by coke deposits. The trade-off between

dx.doi.org/10.1021/cs501279v | ACS Catal. 2015, 5, 438−447

the electron transfer effect and the acid sites effect varies with the TiO_2 content. With the 10 wt % TiO_2 addition, the electron transfer effect of TiO_2 outperforms the acid sites effect and thus better catalytic performance is obtained. With excessive TiO_2 addition (20 and 30 wt %), the acid sites effect of causing excessive coke deposits on the support is more pronounced than the electron transfer effect, which leads to severe deactivation.

A schematic model regarding the influence of TiO_2 on PDH catalytic reaction is proposed (Scheme 1). As shown in Scheme 1, TiO_2 is highly dispersed on the surface of Al_2O_3 upon calcination at 600 °C. After reduction at 500 °C, the partially reduced TiO_x ($x < 2$) species is generated which is catalyzed by platinum. Subsequently, the Pt atoms acquire substantial negative charge from the TiO_x species and some TiO_x species migrate onto metal particle causing partial coverage of metal surface, both of which slightly reduce the initial activity. The electron donation from TiO_x species to Pt atoms hinders propylene adsorption on metal sites and decreases the likelihood of deep dehydrogenation and hydrogenolysis. The increased electron density of Pt atoms also facilitates the migration of coke and coke precursors from active sites to support areas. Less coke-covered Pt particles affords more exposed active sites for PDH. Finally, the electronic effect between Pt and TiO_x species enhances the selectivity to propylene and anti-coking ability remarkably.

Scheme 1. Schematic Model for the Pt/TAx Catalyst and the Role of TiO_2 in Catalytic Performance

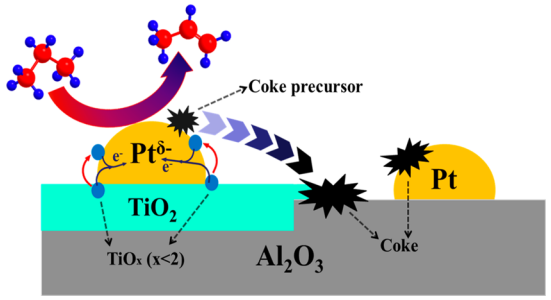

5. CONCLUSIONS

In summary, we have shown that the introduction of TiO_2 has a profound influence on the physical nature and catalytic performance of the catalysts, including increasing propylene selectivity and enhancing the catalytic stability. According to XRD and Raman results, TiO_2 is highly dispersed on the surface of Al_2O_3. Furthermore, the TiO_2 addition leads to the enhancement of support acidity, especially the increase of strong acid centers. The acid sites' effect of high loading TiO_2 causes excessive coke deposits which block the pores other than the active sites. For the active sites, the TiO_2 introduction contributes to the electron donation from partially reduced TiO_x species to Pt, and thus electron-rich Pt particles tend to inhibit the adsorption of propylene and coke precursors, which suppresses the cracking reactions toward lighter hydrocarbons and facilitates the migration of coke and coke precursors from metal surface to the support. Consequently, the electron transfer effect of TiO_2 plays a significant role in improving propylene selectivity as well as catalytic stability. The trade-off between the electron transfer effect and acid sites effect varies with the TiO_2 content. With the 10 wt % TiO_2 addition, the electron transfer effect of TiO_2 outperforms the acid sites effect and thus better catalytic performance is obtained. It is owing to the TiO_2 addition improving the migration of coke deposits/precursors from metal to support and leaving a larger metal surface free. With excessive TiO_2 addition (20 wt %), the acid sites effect of causing excessive coke deposits is more pronounced than the electron transfer effect, which leads to severe deactivation. The optimal loading content of TiO_2 is around 10 wt % on Al_2O_3-supported Pt catalyst, which results in a high propylene selectivity of 89.5% and a better stability.

■ ASSOCIATED CONTENT

Supporting Information

The following file is available free of charge on the ACS Publications website at DOI: 10.1021/cs501279v.

Further results and details are collected in Figures S1 to S3 (PDF)

■ AUTHOR INFORMATION

Corresponding Author

*E-mail: jlgong@tju.edu.cn. Fax: +86-22-87401818.

Notes

The authors declare no competing financial interest.

■ ACKNOWLEDGMENTS

This work was supported by the National Science Foundation of China (21222604, 21206115, and 21376169), the Program for New Century Excellent Talents in University (NCET-10-0611), the Scientific Research Foundation for the Returned Overseas Chinese Scholars (MoE), and the Program of Introducing Talents of Discipline to Universities (B06006).

■ REFERENCES

(1) Santhoshkumar, M.; Hammer, N.; Ronning, M.; Holmen, A.; Chen, D.; Walmsley, J.; Oye, G. *J. Catal.* **2009**, *261*, 116−128.
(2) Santhosh Kumar, M.; Chen, D.; Walmsley, J. C.; Holmen, A. *Catal. Commun.* **2008**, *9*, 747−750.
(3) Azzam, K. G.; Jacobs, G.; Shafer, W. D.; Davis, B. H. *Appl. Catal., A* **2010**, *390*, 264−270.
(4) Baek, J.; Yun, H. J.; Yun, D.; Choi, Y.; Yi, J. *ACS Catal.* **2012**, *2*, 1893−1903.
(5) Ren, Y.; Zhang, F.; Hua, W.; Yue, Y.; Gao, Z. *Catal. Today* **2009**, *148*, 316−322.
(6) Zhang, Y.; Zhou, Y.; Qiu, A.; Wang, Y.; Xu, Y.; Wu, P. *Catal. Commun.* **2006**, *7*, 860−866.
(7) Sokolov, S.; Stoyanova, M.; Rodemerck, U.; Linke, D.; Kondratenko, E. V. *J. Catal.* **2012**, *293*, 67−75.
(8) Bhasin, M. M.; McCain, J. H.; Vora, B. V.; Imai, T.; Pujadó, P. R. *Appl. Catal., A* **2001**, *221*, 397−419.
(9) Zhang, Y.; Zhou, Y.; Huang, L.; Xue, M.; Zhang, S. *Ind. Eng. Chem. Res.* **2011**, *50*, 7896−7902.
(10) Siddiqi, G.; Sun, P.; Galvita, V.; Bell, A. T. *J. Catal.* **2010**, *274*, 200−206.
(11) Bariås, O. A.; Holmen, A.; Blekkan, E. A. *J. Catal.* **1996**, *158*, 1−12.
(12) Larsson, M.; Hultén, M.; Blekkan, E. A.; Andersson, B. *J. Catal.* **1996**, *164*, 44−53.
(13) Iglesias-Juez, A.; Beale, A. M.; Maaijen, K.; Weng, T. C.; Glatzel, P.; Weckhuysen, B. M. *J. Catal.* **2010**, *276*, 268−279.
(14) Nawaz, Z.; Xiaoping, T.; Fei, W. *Korean J. Chem. Eng.* **2009**, *26*, 1528−1532.
(15) Nawaz, Z.; Tang, X.; Wang, Y.; Wei, F. *Ind. Eng. Chem. Res.* **2009**, *49*, 1274−1280.
(16) Han, Z.; Li, S.; Jiang, F.; Wang, T.; Ma, X.; Gong, J. *Nanoscale* **2014**, *6*, 10000−10008.

(17) Sun, P.; Siddiqi, G.; Chi, M.; Bell, A. T. *J. Catal.* **2010**, *274*, 192−199.
(18) Yu, C.; Xu, H.; Ge, Q.; Li, W. *J. Mol. Catal. A: Chem.* **2007**, *266*, 80−87.
(19) Castro, A. A. *Catal. Lett.* **1993**, *22*, 123−133.
(20) Prestvik, R.; Moljord, K.; Grande, K.; Holmen, A. *J. Catal.* **1998**, *174*, 119−129.
(21) Papoian, G.; Nørskov, J. K.; Hoffmann, R. *J. Am. Chem. Soc.* **2000**, *122*, 4129−4144.
(22) Anghel, A. T.; Jenkins, S. J.; Wales, D. J.; King, D. A. *J. Phys. Chem. B* **2006**, *110*, 4147−4156.
(23) Anghel, A. T.; Wales, D. J.; Jenkins, S. J.; King, D. A. *J. Chem. Phys.* **2007**, *126*, 044710−044713.
(24) Watson, G. W.; Wells, R. P. K.; Willock, D. J.; Hutchings, G. J. *J. Phys. Chem. B* **2000**, *104*, 6439−6446.
(25) Airaksinen, S. M. K.; Bañares, M. A.; Krause, A. O. I. *J. Catal.* **2005**, *230*, 507−513.
(26) Casella, M. L.; Siri, G. J.; Santori, G. F.; Ferretti, O. A.; Ramírez-Corredores, M. M. *Langmuir* **2000**, *16*, 5639−5643.
(27) Tasbihi, M.; Feyzi, F.; Amlashi, M. A.; Abdullah, A. Z.; Mohamed, A. R. *Fuel Process. Technol.* **2007**, *88*, 883−889.
(28) Yu, J.; Wang, R.; Ren, S.; Sun, X.; Chen, C.; Ge, Q.; Fang, W.; Zhang, J.; Xu, H.; Su, D. S. *ChemCatChem.* **2012**, *4*, 1376−1381.
(29) Vu, B. K.; Song, M. B.; Ahn, I. Y.; Suh, Y.-W.; Suh, D. J.; Kim, W.-I. L.; Koh, H.-L.; Choi, Y. G.; Shin, E. W. *Catal. Today* **2011**, *164*, 214−220.
(30) Tauster, S. J.; Fung, S. C.; Garten, R. L. *J. Am. Chem. Soc.* **1978**, *100*, 170−175.
(31) Tauster, S. J.; Fung, S. C.; Baker, R. T. K.; Horsley, J. A. *Science* **1981**, *211*, 1121−1125.
(32) Reddy, B. M.; Chowdhury, B.; Reddy, E. P.; Fernández, A. *Langmuir* **2001**, *17*, 1132−1137.
(33) Concepcion, P.; M. Reddy, B.; Knozinger, H. *Phys. Chem. Chem. Phys.* **1999**, *1*, 3031−3037.
(34) Benson, J. E.; Boudart, M. *J. Catal.* **1965**, *4*, 704−710.
(35) Akhtar, M.; Tompkins, F. C. *Trans. Faraday Soc.* **1971**, *67*, 2454−2460.
(36) Redhead, P. A. *Vacuum* **1962**, *12*, 203−211.
(37) Lei, R. Z.; Gellman, A. J.; Koel, B. E. *Surf. Sci.* **2004**, *554*, 125−140.
(38) Serrano-Ruiz, J. C.; Sepúlveda-Escribano, A.; Rodríguez-Reinoso, F. *J. Catal.* **2007**, *246*, 158−165.
(39) Zhaobin, W.; Qin, X.; Xiexian, G.; Sham, E. L.; Grange, P.; Delmon, B. *Appl. Catal.* **1990**, *63*, 305−317.
(40) Overbury, S. H.; Bertrand, P. A.; Somorjai, G. A. *Chem. Rev.* **1975**, *75*, 547−560.
(41) Brugger, P. A.; Mocellin, A. *J. Mater. Sci.* **1986**, *21*, 4431−4435.
(42) Zhou, Z.; Zeng, T.; Cheng, Z.; Yuan, W. *Ind. Eng. Chem. Res.* **2011**, *50*, 883−890.
(43) Zhang, J.; Li, M.; Feng, Z.; Chen, J.; Li, C. *J. Phys. Chem. B* **2005**, *110*, 927−935.
(44) Ohsaka, T.; Izumi, F.; Fujiki, Y. *J. Raman Spectrosc.* **1978**, *7*, 321−324.
(45) Stranick, M. A.; Houalla, M.; Hercules, D. M. *J. Catal.* **1987**, *106*, 362−368.
(46) Huang, W.; Duan, A.; Zhao, Z.; Wan, G.; Jiang, G.; Dou, T.; Chung, K. H.; Liu, J. *Catal. Today* **2008**, *131*, 314−321.
(47) Narayanan, S.; Sultana, A.; Thinh Le, Q.; Auroux, A. *Appl. Catal., A* **1998**, *168*, 373−384.
(48) Lai, Y.; He, S.; Li, X.; Sun, C.; Seshan, K. *Appl. Catal., A* **2014**, *469*, 74−80.
(49) Yang, M.; Men, Y.; Li, S.; Chen, G. *Appl. Catal., A* **2012**, *433−434*, 26−34.
(50) Martín, N.; Viniegra, M.; Lima, E.; Espinosa, G. *Ind. Eng. Chem. Res.* **2004**, *43*, 1206−1210.
(51) Li, Q.; Sui, Z.; Zhou, X.; Zhu, Y.; Zhou, J.; Chen, D. *Top. Catal.* **2011**, *54*, 888−896.
(52) Sanchez, S. I.; Moser, M. D.; Bradley, S. A. *ACS Catal.* **2013**, *4*, 220−228.
(53) Hadjiivanov, K. I.; Klissurski, D. G. *Chem. Soc. Rev.* **1996**, *25*, 61−69.
(54) Yang, M. L.; Zhu, Y. A.; Fan, C.; Sui, Z. J.; Chen, D.; Zhou, X. G. *Phys. Chem. Chem. Phys.* **2011**, *13*, 3257−67.
(55) Nykänen, L.; Honkala, K. *J. Phys. Chem. C* **2011**, *115*, 9578−9586.
(56) Sato, T.; Okaya, K.; Kunimatsu, K.; Yano, H.; Watanabe, M.; Uchida, H. *ACS Catal.* **2012**, *2*, 450−455.
(57) Arteaga, G.; Anderson, J.; Rochester, C. *Catal. Lett.* **1999**, *58*, 189−194.
(58) Huizinga, T.; Prins, R. *J. Phys. Chem.* **1981**, *85*, 2156−2158.
(59) Panagiotopoulou, P.; Kondarides, D. I. *J. Catal.* **2008**, *260*, 141−149.
(60) Vu, B. K.; Song, M. B.; Ahn, I. Y.; Suh, Y.-W.; Suh, D. J.; Kim, W.-I.; Koh, H.-L.; Choi, Y. G.; Shin, E. W. *Appl. Catal., A* **2011**, *400*, 25−33.
(61) Zaera, F. *Prog. Surf. Sci.* **2001**, *69*, 1−98.
(62) Yu, C.; Ge, Q.; Xu, H.; Li, W. *Catal. Lett.* **2006**, *112*, 197−201.
(63) Lieske, H.; Sárkány, A.; Völter, J. *Appl. Catal.* **1987**, *30*, 69−80.
(64) Zhang, Y.; Zhou, Y.; Shi, J.; Zhou, S.; Sheng, X.; Zhang, Z.; Xiang, S. *J. Mol. Catal. A: Chem.* **2014**, *381*, 138−147.